



Thermophotovoltaics with spectral and angular selective doped-oxide thermal emitters

ENAS SAKR^{1,*} AND PETER BERMEL^{1,2}

¹*School of Electrical and Computer Engineering, Purdue University, 456 Northwestern Ave, West Lafayette, IN 47907, USA*

²*Birck Nanotechnology Center, Purdue University, 1205 W State St, West Lafayette, IN 47907, USA*

*esakr@purdue.edu

Abstract: Deliberate control of thermal emission properties using nanophotonics has improved a number of applications including thermophotovoltaics (TPV), radiative cooling and infrared spectroscopy. In this work, we study the effect of simultaneous control of angular and spectral properties of thermal emitters on the efficiencies of TPV systems. While spectral selectivity reduces sub-bandgap losses, angular selectivity is expected to enhance view factors at larger separation distances and hence to provide flexibilities in cooling the photovoltaic converter. We propose a design of an angular and spectral selective thermal emitter based on waveguide perfect absorption phenomena in epsilon-near-zero thin-films. Aluminum-doped Zinc-Oxide is used as an epsilon-near-zero material with a cross-over frequency in the near-infrared. A high contrast grating is designed to restrict the emission in a range of angles around the normal direction, while an integrated filter ensures spectral selectivity to reduce sub-bandgap losses. Theoretical analysis shows an expected relative enhancement of the TPV system efficiency of at least 32% using selective emitters with ideal angular and spectral selectivity at large separation distances compared to a blackbody. This enhancement factor, however, reduces to 3.9% with non-ideal selective emitters. This big reduction of the efficiency is attributed to sub-bandgap losses, off-angular losses and high-temperature dependence of optical constants.

© 2017 Optical Society of America

OCIS codes: (290.6815) Thermal emission; (040.5350) Photovoltaic; (240.0310) Thin films; (050.2770) Gratings.

References and links

1. A. Lenert, D. M. Bierman, Y. Nam, W. R. Chan, I. Celanović, M. Soljačić, and E. N. Wang, "A nanophotonic solar thermophotovoltaic device," *Nat. Nanotechnol.* **9**(2), 126–130 (2014).
2. A. P. Raman, M. A. Anoma, L. Zhu, E. Rephaeli, and S. Fan, "Passive radiative cooling below ambient air temperature under direct sunlight," *Nature* **515**(7528), 540–544 (2014).
3. C. Blanchard, Q. Lévesque, D. Costantini, C. Jomois, J.-L. Leclercq, A.-L. Coutrot, F. Marquier, L. Milord, C. Grillet, H. Benisty, P. Viktorovitch, X. Letartre, and J.-J. Greffet, "Directional and Selective Mid-Infrared Thermal Emitters for Sensing Applications," in *Advanced Photonics 2015* (OSA, 2015), p. SeW2B.2-SeW2B.2.
4. Z. Zhou, E. Sakr, Y. Sun, and P. Bermel, "Solar thermophotovoltaics: Reshaping the solar spectrum," *Nanophotonics* **5**(1), 1–21 (2016).
5. B. Bitnar, W. Durisch, and R. Holzner, "Thermophotovoltaics on the move to applications," *Appl. Energy* **105**, 430–438 (2013).
6. P. Bermel, M. Ghebrehirhan, W. Chan, Y. X. Yeng, M. Araghchini, R. Hamam, C. H. Marton, K. F. Jensen, M. Soljačić, J. D. Joannopoulos, S. G. Johnson, I. Celanovic, M. Soljacic, and I. Celanovic, "Design and global optimization of high-efficiency thermophotovoltaic systems," *Opt. Express* **18**(S3), A314–A334 (2010).
7. M. F. Modest, *Radiative Heat Transfer* (Academic, 2013).
8. E. Sakr, D. Dimonte, and P. Bermel, "Metasurfaces with Fano resonances for directionally selective thermal emission," *MRS Adv.* **1**(49), 3307–3316 (2016).
9. W. R. Chan, P. Bermel, R. C. N. Pilawa-Podgurski, C. H. Marton, K. F. Jensen, J. J. Senkevich, J. D. Joannopoulos, M. Soljacic, and I. Celanovic, "Toward high-energy-density, high-efficiency, and moderate-temperature chip-scale thermophotovoltaics," *Proc. Natl. Acad. Sci. U.S.A.* **110**(14), 5309–5314 (2013).
10. W. M. Yang, S. K. Chou, C. Shu, H. Xue, and Z. W. Li, "Development of a prototype micro-thermophotovoltaic power generator," *J. Phys. Appl. Phys.* **37**(7), 1017–1020 (2004).

11. W. M. Yang, S. K. Chou, J. F. Pan, J. Li, and X. Zhao, "Comparison of cylindrical and modular micro combustor radiators for micro-TPV system application," *J. Micromech. Microeng.* **20**(8), 85003 (2010).
12. C. Wu, B. Neuner III, J. John, A. Milder, B. Zollars, S. Savoy, and G. Shvets, "Metamaterial-based integrated plasmonic absorber/emitter for solar thermo-photovoltaic systems," *J. Opt.* **14**(2), 024005 (2012).
13. L. M. Fraas, J. E. Avery, and H. X. Huang, "Thermophotovoltaic furnace-generator for the home using low bandgap GaSb cells," *Semicond. Sci. Technol.* **18**(5), S247–S253 (2003).
14. Z. Zhou, X. Sun, and P. Bermel, "Radiative cooling for thermophotovoltaic systems," *Proc. SPIE* **9973**, 997308 (2016).
15. X. Sun, T. J. Silverman, Z. Zhou, M. R. Khan, P. Bermel, and M. A. Alam, "An Optics-Based Approach to Thermal Management of Photovoltaics: Selective-Spectral and Radiative Cooling," *IEEE J. Photovolt.* **7**(2), 566–574 (2017).
16. H. Chung, Z. Zhou, and P. Bermel, "Collimated thermal radiation transfer via half Maxwell's fish-eye lens for thermophotovoltaics," *Appl. Phys. Lett.* **110**(20), 201111 (2017).
17. D. L. D. Chubb, A. T. A. Pal, M. M. O. Patton, and P. P. P. Jenkins, "Rare earth doped high temperature ceramic selective emitters," *J. Eur. Ceram. Soc.* **19**(13–14), 2551–2562 (1999).
18. G. E. Guazzoni, "High-Temperature Spectral Emittance of Oxides of Erbium, Samarium, Neodymium and Ytterbium," *Appl. Spectrosc.* **26**(1), 60–65 (1972).
19. E. S. Sakr, Z. Zhou, and P. Bermel, "High efficiency rare-earth emitter for thermophotovoltaic applications," *Appl. Phys. Lett.* **105**(11), 111107 (2014).
20. K. A. Arpin, M. D. Losego, A. N. Cloud, H. Ning, J. Mallek, N. P. Sergeant, L. Zhu, Z. Yu, B. Kalanyan, G. N. Parsons, G. S. Girolami, J. R. Abelson, S. Fan, and P. V. Braun, "Three-dimensional self-assembled photonic crystals with high temperature stability for thermal emission modification," *Nat. Commun.* **4**, 2630 (2013).
21. J.-J. Greffet, R. Carminati, K. Joulain, J.-P. Mulet, S. Mainguy, and Y. Chen, "Coherent emission of light by thermal sources," *Nature* **416**(6876), 61–64 (2002).
22. M. Laroche, C. Arnold, F. Marquier, R. Carminati, J.-J. Greffet, S. Collin, N. Bardou, and J.-L. Pelouard, "Highly directional radiation generated by a tungsten thermal source," *Opt. Lett.* **30**(19), 2623–2625 (2005).
23. G. Biener, N. Dahan, A. Niv, V. Kleiner, and E. Hasman, "Highly coherent thermal emission obtained by plasmonic bandgap structures," *Appl. Phys. Lett.* **92**(8), 081913 (2008).
24. M. De Zoysa, T. Asano, K. Mochizuki, A. Oskooi, T. Inoue, and S. Noda, "Conversion of broadband to narrowband thermal emission through energy recycling," *Nat. Photonics* **6**(8), 535–539 (2012).
25. D. Costantini, A. Lefebvre, A.-L. Coutrot, I. Moldovan-Doyen, J.-P. Hugonin, S. Boutami, F. Marquier, H. Benisty, and J.-J. Greffet, "Plasmonic Metasurface for Directional and Frequency-Selective Thermal Emission," *Phys. Rev. Appl.* **4**(1), 014023 (2015).
26. E. Sakr and P. Bermel, "Angle-Selective Reflective Filters for Exclusion of Background Thermal Emission," *Phys. Rev. Appl.* **7**(4), 044020 (2017).
27. A. Alù, M. G. Silveirinha, A. Salandrino, and N. Engheta, "Epsilon-near-zero metamaterials and electromagnetic sources: Tailoring the radiation phase pattern," *Phys. Rev. B* **75**(15), 155410 (2007).
28. J. Kim, A. Dutta, G. V. Naik, A. J. Giles, F. J. Bezares, C. T. Ellis, J. G. Tischler, A. M. Mahmoud, H. Caglayan, O. J. Glembocki, A. V. Kildishev, J. D. Caldwell, A. Boltasseva, and N. Engheta, "Role of epsilon-near-zero substrates in the optical response of plasmonic antennas," *Optica* **3**(3), 339 (2016).
29. B. Edwards, A. Alù, M. E. Young, M. Silveirinha, and N. Engheta, "Experimental Verification of Epsilon-Near-Zero Metamaterial Coupling and Energy Squeezing Using a Microwave Waveguide," *Phys. Rev. Lett.* **100**(3), 033903 (2008).
30. A. M. Mahmoud and N. Engheta, "Wave-matter interactions in epsilon-and-mu-near-zero structures," *Nat. Commun.* **5**, 5638 (2014).
31. V. E. Babicheva, N. Kinsey, G. V. Naik, M. Ferrera, A. V. Lavrinenko, V. M. Shalaev, and A. Boltasseva, "Towards CMOS-compatible nanophotonics: Ultra-compact modulators using alternative plasmonic materials," *Opt. Express* **21**(22), 27326–27337 (2013).
32. S. Vassant, J.-P. Hugonin, F. Marquier, and J.-J. Greffet, "Berreman mode and epsilon near zero mode," *Opt. Express* **20**(21), 23971–23977 (2012).
33. S. Campione, I. Brener, and F. Marquier, "Theory of epsilon-near-zero modes in ultrathin films," *Phys. Rev. B – Condens. Matter Mater. Phys.* **91**(12), 1–5 (2015).
34. G. V. Naik, J. Kim, and A. Boltasseva, "Oxides and nitrides as alternative plasmonic materials in the optical range [Invited]," *Opt. Mater. Express* **1**(6), 1090 (2011).
35. R. Maas, J. Parsons, N. Engheta, and A. Polman, "Experimental realization of an epsilon-near-zero metamaterial at visible wavelengths," *Nat. Photonics* **7**(11), 907–912 (2013).
36. E. Feigenbaum, K. Diest, and H. A. Atwater, "Unity-order index change in transparent conducting oxides at visible frequencies," *Nano Lett.* **10**(6), 2111–2116 (2010).
37. J. Park, J.-H. Kang, X. Liu, and M. L. Brongersma, "Electrically tunable epsilon-near-zero (ENZ) metafilm absorbers," *Sci. Rep.* **5**(1), 15754 (2015).
38. S. Vassant, I. Moldovan Doyen, F. Marquier, F. Pardo, U. Gennser, A. Cavanna, J. L. Pelouard, and J. J. Greffet, "Electrical modulation of emissivity," *Appl. Phys. Lett.* **102**(8), 1–4 (2013).
39. V. W. Brar and M. C. Sherrott, L. Sweatlock, M. S. Jang, L. Kim, M. Choi, and H. Atwater, "Electronic modulation of infrared emissivity in graphene plasmonic resonators," *Nat. Commun.* **6**, 1–7 (2015).

40. T. Inoue, M. De Zoysa, T. Asano, and S. Noda, "Realization of dynamic thermal emission control," *Nat. Mater.* **13**(10), 928–931 (2014).
41. V. Karagodsky, F. G. Sedgwick, and C. J. Chang-Hasnain, "Theoretical analysis of subwavelength high contrast grating reflectors," *Opt. Express* **18**(16), 16973–16988 (2010).
42. E. Sakr and P. Bermel, "Spectral and angular-selective thermal emission from gallium-doped zinc oxide thin film structures," in (2017), Vol. 10099, p. 100990A–100990A–8.
43. J. N. Winn, Y. Fink, S. Fan, and J. D. Joannopoulos, "Omnidirectional reflection from a one-dimensional photonic crystal," *Opt. Lett.* **23**(20), 1573–1575 (1998).
44. F. A. F. and E. M. J. Rivera, "Plasmonics - Principles and Applications," in K. Y. Kim, ed. (InTech, 2012).
45. P. Berini, "Long-range surface plasmon polaritons," *Adv. Opt. Photonics* **1**(3), 484–588 (2009).
46. C. Kittel, *Introduction to Solid State Physics* (Wiley, 2005).
47. R. A. Ferrell, "Predicted Radiation of Plasma Oscillations in Metal Films," *Phys. Rev.* **111**(5), 1214–1222 (1958).
48. D. W. Berreman, "Infrared Absorption at Longitudinal Optic Frequency in Cubic Crystal Films," *Phys. Rev.* **130**(6), 2193–2198 (1963).
49. W. D. Newman, C. L. Cortes, J. Atkinson, S. Pramanik, R. G. DeCorby, and Z. Jacob, "Ferrell–Berreman Modes in Plasmonic Epsilon-near-Zero Media," *ACS Photonics* **2**(1), 2–7 (2015).
50. T. S. Luk, S. Campione, I. Kim, S. Feng, Y. C. Jun, S. Liu, J. B. Wright, I. Brener, P. B. Catrysse, S. Fan, and M. B. Sinclair, "Directional perfect absorption using deep subwavelength low-permittivity films," *Phys. Rev. B* **90**(8), 085411 (2014).
51. S. E. Han, "Theory of thermal emission from periodic structures," *Phys. Rev. B* **80**(15), 155108 (2009).
52. V. Liu and S. Fan, "S4 : A free electromagnetic solver for layered periodic structures," *Comput. Phys. Commun.* **183**(10), 2233–2244 (2012).
53. P. Bermel, W. Chan, Y. X. Yeng, J. D. Joannopoulos, M. Soljacic, and I. Celanovic, "Design and global optimization of high-efficiency thermophotovoltaic systems," in *TPV9: Ninth World Conference on Thermophotovoltaic Generation of Electricity* (2010).
54. M. A. Green, "Solar cell fill factors: general graph and empirical expressions," *Solid-State Electron.* **24**(8), 788–789 (1981).
55. G. V. Naik, V. M. Shalaev, and A. Boltasseva, "Alternative Plasmonic Materials: Beyond Gold and Silver," *Adv. Mater.* **25**(24), 3264–3294 (2013).
56. M. Garin, D. Hernández, T. Trifonov, and R. Alcubilla, "Three-dimensional metallo-dielectric selective thermal emitters with high-temperature stability for thermophotovoltaic applications," *Sol. Energy Mater. Sol. Cells* **134**, 22–28 (2015).
57. L. H. Sperling, *Introduction to Physical Polymer Science* (John Wiley & Sons, 2005).
58. L. Zhao, S. Yang, B. Bhatia, E. Strobach, and E. N. Wang, "Modeling silica aerogel optical performance by determining its radiative properties," *AIP Adv.* **6**, 025123 (2016).
59. W. J. Tropf, "Temperature-dependent refractive index models for BaF₂, CaF₂, MgF₂, SrF₂, LiF, NaF, KCl, ZnS, and ZnSe," *Opt. Eng.* **34**(5), 1369–1373 (1995).
60. P. J. Timans, "Emissivity of silicon at elevated temperatures," *J. Appl. Phys.* **74**(10), 6353–6364 (1993).
61. H. Reddy, U. Guler, A. V. Kildishev, A. Boltasseva, and V. M. Shalaev, "Temperature-dependent optical properties of gold thin films," *Opt. Mater. Express* **6**(9), 2776–2802 (2016).
62. K. Ujihara, "Reflectivity of Metals at High Temperatures," *J. Appl. Phys.* **43**(5), 2376–2383 (1972).

1. Introduction

Thermal emitters are usually incoherent sources that lack spectral selectivity and directivity. There can be considerable benefits to deviating from this state, however. Deliberate control of thermal emission spectra has enabled a number of applications, including thermophotovoltaics (TPV) [1], daytime radiative cooling [2] and sensing applications [3]. TPV is a method for directly converting thermal radiation into electricity, where thermal photons radiated by an emitter heated up to 1500 K are converted to electricity using a low-bandgap photovoltaic device [4]. Only photons with energies above the TPV bandgap are converted into electricity. Consequently, spectral matching between the emitted heat and the TPV diode is necessary to enhance conversion efficiencies [5,6]. On the other hand, the lack of directivity of the thermal emitter requires placing it close enough to the TPV diode, to increase the portion of the received photons at the diode. The view factor or the form factor [7] quantifies this portion. It can be shown that the view factor approaches unity for planar structures with lateral dimensions much larger than the separation distance [8], as well as for concentric cylindrical structures [5]. The former case is particularly effective for modular and compact TPV devices, such as micro-TPV generators [9–11], while the latter is effective for

larger scale solar-TPV devices such as the structure suggested in [12], or TPV generator prototypes developed by JX Crystals Inc [13].

In both cases, the TPV diode should be efficiently cooled to temperatures close to room temperature, to avoid significant losses from heat-induced bandgap shrinking, which increases its dark current [14]. Furthermore, effective cooling of the diode increases its lifetime and reliability [15]. However, with the TPV device included in vacuum encapsulation to minimize convection losses, maintaining the TPV diode at appropriate temperatures is challenging. Alternatively, controlling the directivity of the thermal emission may offer a solution to this problem, by collimating the radiated heat towards the diode converter. Hence, a high view factor can still be maintained between the emitter and a distant receiver. This design may allow one to remove the TPV diode from the vacuum encapsulation, and thus provide a greater flexibility in cooling the converter using passive cooling techniques [16].

Based on this discussion, controlling both the spectral and directional selectivities of thermal emission may offer greater flexibility in the TPV system design. As for spectral control, several methods have been established to shape the emission spectrum, including naturally-selective materials such as rare-earth oxides and doped ceramics [17–19], and engineered photonic and plasmonic structures [1,12,20]. For directional control of thermal emission, it can be modified using engineered structures like metallic gratings and metasurfaces [21,22]. Furthermore, combining spectral selectivity and angular selectivity has been also demonstrated using highly coherent plasmonic bandgap structures [23], or by coupling spectrally-selective emitters to angular selective surfaces [24–26]. For example, by coupling quantum dot emission modes to photonic crystals [24], coupling gap plasmon resonances to periodic metallic gratings [25], or coupling naturally-selective emitters to guided mode resonant filters [26].

In this work, we propose a distinctive method to simultaneously control the spectral selectivity and directivity of thermal emission using epsilon-near zero (ENZ) thin-film structures. In ENZ materials, the permittivity function crosses zero, and the wave can propagate with no phase advance or delay. ENZ-based structures have recently found many applications, such as energy squeezing, radiation pattern engineering, controlling spontaneous emission, and compact optical modulators [27–31]. Furthermore, ultrathin films of ENZ materials exhibit nearly perfect absorption, following the special dispersion characteristics near the ENZ regime [32,33]. Materials that exhibit ENZ behavior include metals, with their zero-crossing wavelengths in the ultraviolet, transparent conducting oxides in the near infrared [34], and polar dielectrics and doped semiconductors in the mid-infrared [32]. In general, metamaterials provide flexibility in shifting the ENZ regime to targeted optical wavelength ranges [35].

Furthermore, utilizing ENZ thin-films in designing thermal emitters provides a method to actively control thermal radiation through voltage tuning. When the emitter is placed far enough from the receiver, the system is vulnerable to angular misalignments, which may result from time-varying input heat causing changes in the emission spectrum, as well as mechanical effects like vibration, thermal expansion and contraction. Active tuning of thermal emission provides a method to proactively address such problems, to maintain high selectivity in both angular and spectral domains across a wide range of conditions. Structures for room-temperature active control of reflectivity and absorptivity using this class of materials have already been proposed and experimentally demonstrated [36,37]. Also, electrical modulation of thermal emission intensity and frequency was demonstrated using ENZ modes in thin films [38] and alternative methods such as graphene micro-resonators [39] and quantum well photonic crystal structures [40]. Nonetheless, except for [40], the observed high-temperature modulation was weak compared to room-temperature measurements, possibly because of experimental challenges and high-temperature mechanical effects. Hence, optimized designs of photonic structures using ENZ thin films could yield more pronounced

modulation of the spectrum, direction and intensity of thermal emissivity, subject to experimental and design constraints.

Our approach utilizes this perfect absorption phenomena in transparent conducting oxides to design nearly perfect spectrally selective emitters. Coupling to this mode through a high-contrast grating [41] also provides angular selectivity. In a previous work [42], we investigated this design for TPV system efficiency enhancement. Here, we extend our design to couple to both *s*- and *p*-polarized modes. The details of the different absorption mechanisms present here are explained. We then employ this design as an emitter in a TPV system, to theoretically investigate the potential efficiency enhancement with angularly- and spectrally-selective thermal emission. Finally, we compare the performance to an ideal selective emitter and investigate the effect of sub-bandgap losses and off-angular emission losses.

2. Theory

As mentioned above, the suggested TPV system consists of a spectrally-selective thermal emitter of infinite extension in one direction, and a length l_1 in the other direction. The selective emitter radiates directive emission towards a TPV cell located at an arbitrary distance D . The TPV cell array is assumed to have infinite extension in one dimension and a length l_2 in the other dimension. We assume that $l_1 = l_2 = L$ in our subsequent calculations. Figure 1 demonstrates the proposed TPV setup.

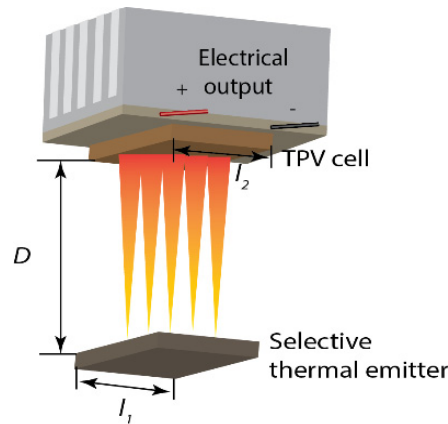


Fig. 1. A TPV system with a directional and frequency-selective thermal emitter placed on an arbitrary distance from the PV converter. The selectivity of the emitter maintains high thermal-to-electrical energy conversion efficiency at larger separation distances.

The selective emitter structure is depicted in Fig. 2. The core design lies in the bottom section of the emitter, where a thin ENZ film of thickness t_{ENZ} is backed by a metal to support surface modes excited in the thin film. The top surface is covered by an array of square patches of dimensions $w_x = w_y = w$, made of a high-index material, typically Si. The grating thickness is t_g , and its periodicity is $a_x = a_y = a$. This bottom structure by itself supports selective absorption modes with directivity dictated by the grating. The 2D periodicity of the grating ensures coupling of both *s*-polarized and *p*-polarized incident modes to absorption modes in the ENZ thin-film. To selectively exclude longer-wavelength modes, an omnidirectional 1D photonic crystal (PhC) filter [43] is placed at a distance t_{gap} in the order of a few wavelengths. In the following discussion, a detailed description of the underlying physics of the selective absorption is presented. These absorption modes are ENZ mode, Ferrell-Berremann mode, and waveguide perfect absorption mode. Angular selectivity of the grating coupler and frequency selectivity are also discussed.

2.1 Absorption modes in ENZ thin-films

A thick metal film supports delocalized surface plasmon polariton (SPP) modes at its interface with a semi-infinite dielectric medium for p -polarized modes [44]. Inside the dielectric and the metallic media, the magnetic field profile decays exponentially away from the interface, with a larger decay factor inside the metal. The dispersion characteristics of this SPP mode is given by $k_p = k_0 \sqrt{\epsilon_m \epsilon_d / (\epsilon_m + \epsilon_d)}$, where k_p is the parallel wavevector of the plasmonic mode, k_0 is the wavevector in space, and ϵ_m and ϵ_d are the relative permittivities of the metal and the dielectric, respectively. This dispersion relation lies entirely below the light line when the real part of ϵ_m is negative, and shows an asymptote near the SPP frequency satisfying $\text{Re}\{\epsilon_m\} = -\epsilon_d$. Exciting these modes from free space requires couplers like the Otto and Kretschmann configurations. The characteristics however lies entirely above the light line when the real part of ϵ_m is positive. For metals, the real part of the permittivity crosses zero at a frequency in the ultraviolet range. For TPV thermal emission applications, we use transparent conducting oxides with cross-over frequencies in the near-IR regime, as controlled by the deposition and doping conditions [34].

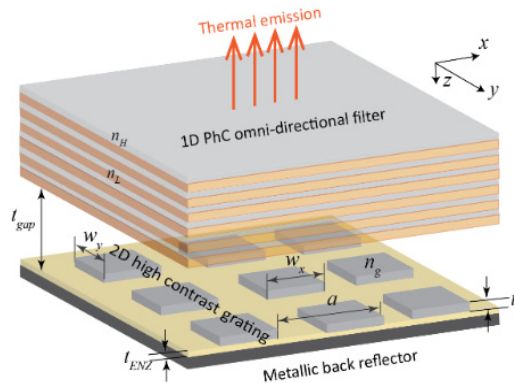


Fig. 2. The structure of an angular and spectral selective thermal emitter, based on thin-film doped-oxides. The bottom structure is an ENZ thin film material on a metallic reflector, and a 2D high contrast grating on top for coupling. The top structure is a 1D dielectric stack of alternating high- and low-index materials n_H and n_L .

2.1.1 ENZ mode

By making a thin film, two SPP modes can now be supported at both the top and the bottom interfaces. When it is thin enough, the decaying SPP modes interact with each other forming symmetric (even) and anti-symmetric (odd) modes. Thus the SPP branch separates into two branches, called also the short-range SPP (SRSP) and the long-range SPP (LRSP) modes according to their decay factor [45]. For thinner films, the LRSP mode shows an asymptote near the cross-over frequency. This mode is called the ENZ mode [33]. With a metallic support at the back, the ENZ mode propagates in the thin film and eventually will be totally absorbed.

2.1.2 Ferrell-Berremann mode

As the permittivity function crosses zero from negative to positive values, the thin film becomes a low-index dielectric with permittivity values less than unity. Hence, the supported modes are p -polarized radiative modes, and can be excited from air. The nature of the excited mode resembles collective volumetric oscillating electrons inside the thin film, known as a volume-plasmon mode [46]. Historically, this mode was observed in thin metallic films by Ferrell [47], and in polar dielectrics by Berremann [48]. Thus we denote this mode as Ferrell-

Berremian mode, following the notation in [49]. A detailed analysis of the full dispersion characteristics of the ENZ mode and the Berremian mode can be found in [32].

2.1.3 Waveguide perfect absorption (PA) mode

With the presence of a metallic interface at the bottom, e.g. tantalum, it is possible to couple to a perfect absorption mode (PA), characterized by a resonance below the light line. It is efficiently coupled from air through a grating or a prism coupler [50], and is associated with a near-zero positive permittivity function. Directional PA is observed in [50] using a glass prism coupler. The PA arises at or beyond the critical angle between the high-index medium (glass) and the ENZ medium [indium-doped tin-oxide (ITO)]. The resonance peaks depend on the ITO film's thickness, corresponding to when the mode is completely confined in the ITO.

2.2 Angle restriction mechanism

From the previous discussion, it appears that both radiative and non-radiative modes can exist in the structure. A grating coupler can be used to differentiate between them by the light line of the grating. With careful selection of the grating's period, one can confine the absorption cone to a specific angle governed by the grating's light line. This critical angle is given by $\theta_c = \arcsin(1 - \lambda/a)$, where λ is the wavelength, and a is the period. Accordingly, we choose λ to be the cross-over frequency, to approximately control the confinement angle. Since all the three modes mentioned in section 2.1 exist around the cross-over frequency, we design the grating to restrict the angle of the highest frequency mode (the PA mode) to ensure directivity for most frequencies involved above the TPV bandgap.

2.3 Frequency selectivity

Although the proposed design restricts the absorption angle for the PA mode, Ferrell-Berremian and ENZ modes also still exist at longer wavelengths. These modes are regarded here as parasitic sub-bandgap emission that reduces the efficiency of the TPV system, which should be eliminated. In fact, this is the purpose of the top omni-directional filter shown in Fig. 2. The design of this filter should also maintain an angular-independent narrowband transmission selectivity for the PA mode for both polarization states. The filter is placed close to the bottom structure but not directly on top, to avoid altering the optical response of the bottom structure. Thus, we choose to add an air gap between the top and the bottom structures, with a thickness on the order of a few wavelengths.

3. Methodology

In this section, we present the computational methods used to calculate selective emissivity functions and the TPV system efficiency.

3.1 Emissivity computation

We use Kirchhoff's law of thermal radiation to compute the emissivity [51]. For an arbitrary body at thermal equilibrium, the emissivity equals absorptivity for a given wavelength, incident angle and state of polarization $\epsilon^{ps}(\lambda, \theta) = A^{ps}(\lambda, \theta)$. Since power balance should be maintained, then $A^{ps}(\lambda, \theta) = 1 - R^{ps}(\lambda, \theta) - T^{ps}(\lambda, \theta)$, where $R^{ps}(\lambda, \theta)$ and $T^{ps}(\lambda, \theta)$ are the reflectivity and the transmissivity under the same condition. To compute the reflectivity and transmissivity functions, we use S⁴ [52], a freely available software, that performs frequency domain computation, based on the Fourier modal method (FMM) coupled to the S-matrix approach.

Our emissivity computation assumes an incident wave in the x - z plane, with mixed polarization. For simplicity, we assume the emitter has infinite extension in the y -direction.

This assumption requires only computation of the emissivity in the x - z plane (i.e. with the azimuthal angle fixed at 0). This assumption simplifies the view factor computation and the TPV efficiency as a result. However, accurate modeling of the dependence of the azimuthal angle, as well as the view factor computation may be necessary to precisely calculate the solid angle of emission in a cone around the normal direction.

3.2 TPV efficiency calculation

The TPV system efficiency can be estimated as the portion of the total emitted power that is converted to electric power:

$$\eta = V_{OC} I_{SC} FF / P_{em}, \quad (1)$$

where V_{OC} , FF , I_{SC} , and P_{em} are the open-circuit voltage, the fill-factor, the short-circuit current and the total emitted power in the upper hemisphere above the emitter. We use the standard calculation method presented in [6,42,53], taking the directional properties of the emitted radiation into consideration. A semi-infinite structure is chosen to provide a mathematically-tractable system to accurately estimate TPV efficiency. The short-circuit current in presence of directive emission can be computed in terms of $\phi_r(\lambda)$, the received normalized power at the TPV diode, which is given by:

$$\phi_r(\lambda) = \int_{x_1=-l_1/2}^{l_1/2} dx_1 \int_{x_2=-l_2/2}^{l_2/2} dx_2 \varepsilon^{ps}(\lambda, x_1, x_2) \frac{D^2}{2(D^2 + x_1^2 + x_2^2 - 2x_1x_2)^{3/2}}, \quad (2)$$

where $\varepsilon^{ps}(\lambda, x_1, x_2)$ is the emissivity function that depends on the wavelength and the emitter's and the receiver's coordinates x_1 and x_2 , respectively. $\varepsilon^{ps}(\lambda, x_1, x_2)$ can be computed directly from the angular dependent emissivity function $\varepsilon^{ps}(\lambda, \theta)$ using the transformation $\tan \theta = (x_1 - x_2)/D$. The right-hand side in (2) integrates the total emitted power from an emitter stripe of width l_1 that is intercepted by a stripe of width l_2 located at a distance D . The geometric factor $D^2/2(D^2 + x_1^2 + x_2^2 - 2x_1x_2)^{3/2}$ is the transformation of the view factor equation [7] in a single dimension of the Cartesian coordinates. The short-circuit current can then be computed using the following formula:

$$I_{SC} = A_d \int_0^{\lambda_g} d\lambda \frac{2qc}{\lambda^4} \frac{\phi_r(\lambda) EQE(\lambda)}{\exp(hc/\lambda kT_e) - 1}, \quad (3)$$

where λ is the wavelength, λ_g is the bandgap wavelength of the TPV diode, A_d is the diode's surface area, q is the electron charge, c is the speed of light, h is Planck's constant, k is Boltzmann's constant and T_e is the emitter's temperature in K. For simplicity, we assume the external quantum efficiency of the diode $EQE(\lambda)$, is uniform for wavelengths below λ_g . Then, the open-circuit voltage is computed from Shockley diode equation [46], and the fill-factor is computed from empirical relations [54]. Finally, the emitted power from an area A_{em} is the total integrated power in the upper hemisphere, and it also accounts for the directional properties of the emitter through the function $\phi_{em}(\lambda)$:

$$P_{em} = A_{em} \int_0^{\infty} d\lambda \frac{2hc^2}{\lambda^5} \frac{\phi_{em}(\lambda)}{\exp(hc/\lambda kT_e) - 1}, \quad (4)$$

$$\phi_{em}(\lambda) = \int_{x_1=-l_1/2}^{l_1/2} dx_1 \int_{x_2=-\infty}^{\infty} dx_2 \varepsilon^{ps}(\lambda, x_1, x_2) \frac{D^2}{2(D^2 + x_1^2 + x_2^2 - 2x_1x_2)^{3/2}}. \quad (5)$$

4. Results

In this section, the spectral and angular selective emissivity of the structure in Fig. 2 is presented. First, we study the emissivity of the bottom structure in Fig. 2, excluding the filter. This analysis will identify the different absorption mechanisms near the cross-over frequency. Once the PA mode is identified, we then proceed to design the top omni-directional filter, and finally we compute the expected TPV system efficiency as described in the previous section.

4.1 Emissivity function excluding the filter

The bottom structure of Fig. 2 consists of a thin film of an ENZ material backed by a metal and topped by a grating coupler. We choose Aluminum-doped Zinc-Oxide (AZO) as the ENZ material due to its low damping factor. The AZO is modeled using a Drude model with parameters obtained from [55]. The metal in the back is chosen to be Tantalum because of its low parasitic losses, and is also modeled using a Lorentz-Drude fit over the range of wavelengths of interest. All the parameters are normalized to the period of the grating a , which is selected to be 900 nm. The thickness of the AZO layer is $0.05a$, and the thickness of the grating is $0.1a$, with $w = 0.534a$. The cross-over frequency of the selected AZO model is located at 1336 nm, or around $0.674(c/a)$ in normalized frequency units.

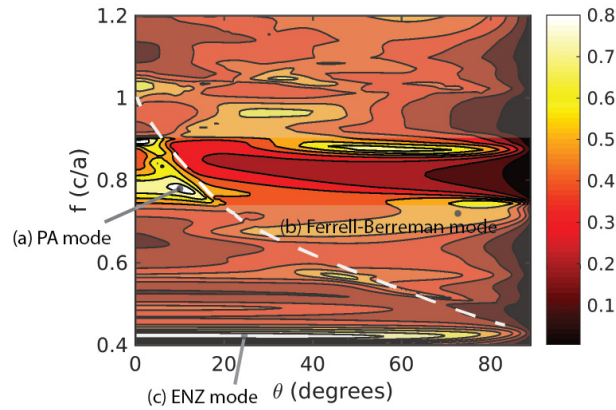


Fig. 3. Emissivity of the bottom structure in Fig. 2 (without the filter), as a function of the incident angle and the normalized frequency. Parameters used are $a_x = a_y = a$, $w_x = w_y = w = 0.543a$, $t_g = 0.1a$, $t_{ENZ} = 0.05a$, and $a = 900$ nm. The ENZ thin-film is made of AZO, and the bottom metal is Ta. Perfect absorption modes, Ferrell-Berremann modes, and ENZ modes are all observed. The dashed line represents the grating light line $\theta_c = \text{asin}(1 - \lambda/a)$. The fully transparent window ($f = 0.7-0.9$ c/a) shows the desired emission spectrum selected by the top filter in Fig. 2.

The simulation scans the emissivity frequency response over a range of incident angles from 0° to 89° . A contour plot of the emissivity as a function of the normalized frequency and the emission angle is shown in Fig. 3. Three high-emissivity modes can be identified around the cross-over frequency:

1. Near PA mode about $0.8c/a$, with a restricted emission angle of $\sim 18^\circ$. This mode is coupled efficiently below the grating light line (dashed-white line in Fig. 3). At this frequency (1125 nm), the real part of the permittivity function is positive and equals $1.191 + 0.1012i$.

2. Ferrell-Berremann mode about $0.7c/a$. This mode is coupled above the light line of the grating, since it is a radiative mode as discussed in section 2.1.2. The absorptivity is less strong around this regime, since the coupled Ferrell-Berremann resonance can still radiate back in air through reverse grating coupling. At this frequency (1143 nm) the real part of the permittivity function is also positive, but less than one, and equals $0.9505 + 0.107i$.
3. ENZ mode about $0.42c/a$. This mode is coupled below the grating light line, hence at this frequency, it extends over most of the angular range. At this frequency (2142 nm) the real part of the permittivity is negative and equals $-5.516 + 0.7108i$.

4.2 Mechanisms of absorption

To confirm the physical origin of each mode, we plot the field distributions for each mode. Figure 4 shows the three electric field components at three different points on the contour plot in Fig. 3, labeled as a, b, and c. Each point corresponds to one of the distinctive absorption modes defined around the cross-over frequency as discussed earlier:

- Point (a) is at a normalized frequency value of $0.7759c/a$, and an incident angle of 11° . This point is expected to show a PA mode. The fields plot in Fig. 4(a) confirms coupling of the incident field components into an E_z component inside the AZO thin-film with minimal reflection in air. As a result, the coupled field will be guided in the thin film, and almost completely absorbed in the AZO layer.
- Point (b) is at a normalized frequency value of $0.6977c/a$, and an incident angle of 64° . At this point, the resonant field profile in the AZO layer is evident. This absorption mode is due to Ferrell-Berremann behavior, that can be coupled directly from p -polarized incidence from air. Because of the grating coupling, the resonant mode can radiate back in air, causing increased reflection and reduced absorption.
- Point (c) is at a normalized frequency value of $0.4206c/a$, and an incident angle of 25° . Below the light line, surface waves are coupled near the AZO-grating interface. The plotted field show decaying field profiles inside the grating and air for the z -component. This behavior is similar to an SPP propagating at a metal-dielectric interface.

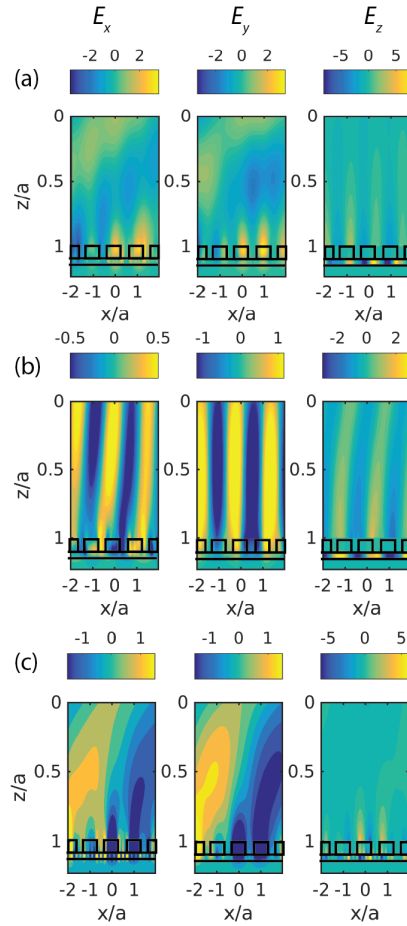


Fig. 4. Electric field profiles of E_x , E_y and E_z showing enhanced fields inside the AZO thin film, resulting in nearly perfect absorption. Plots are taken at different points labeled in Fig. 3: (a) Perfect absorption mode due to coupling to a waveguide mode. (b) Absorption caused by excitation of Ferrell-Berremann mode coupled above the grating light line. (c) Absorption caused by ENZ mode excitation in the thin film with decaying field profiles inside the grating.

4.3 Filter design

The contour plot in Fig. 3 includes omni-directional components that will add extra parasitic losses to the system. To isolate the PA mode with directional and frequency selectivity, an omni-directional filter is designed to filter out other modes. To design a filter with feasible parameters, we first reduce the AZO thickness to $0.03a$ to pull the ENZ mode closer to the cross-over frequency [32]. Accordingly, it is possible to design a filter with a narrow, omni-directional transmission band around $0.8c/a$. The designed filter is $A(0.5L)(HL)^8(0.5L)A$, where L and H indicate low- and high-index materials with indices $n_H = 3.6$, and $n_L = 1.37$, respectively, and A indicates air or vacuum. These refractive indices values can be realized using Si and MgF_2 materials system. Thicknesses of alternating layers are $d_H = a/6.4$ and $d_L = a/3.2$, while the thickness of the top and the bottom layer is $d_L/2$. The filter is placed at a distance $t_{gap} = 4a$. The purpose of this gap distance is to avoid direct interference at the filter-grating interface, thus allowing the filter to function properly without altering the AZO emissivity response. The emissivity function of the full structure in Fig. 2 is plotted in Fig. 5, showing a directional mode around $0.78c/a$ with angular restriction of 18° . Comparison of the bottom structure only (Fig. 3) with the bottom structure in the presence of the filter (Fig. 5)

shows that the filter only isolates targeted modes, without altering the optical response in this wavelength range.

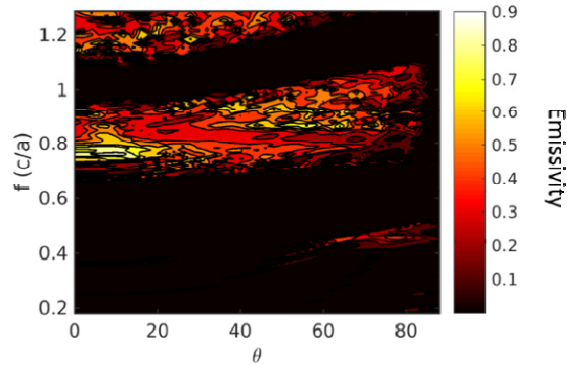


Fig. 5. The emissivity function of the full emitter structure in Fig. 2. The selected ENZ material is AZO of thickness $t_{ENZ} = 0.03a$, with optical parameters retrieved from [55] with a Tantalum back reflector and a Si grating. The filter is design as $A(0.5L)(HL)^8(0.5L)A$, with $n_H = 3.6$, $n_L = 1.37$, and $d_L/d_H = 0.8/1.6$. The separation gap is $t_{gap} = 4a$, with $a = 900$ nm. A selective emission of angular half-width of 18° around $f = 0.78c/a$ is evident.

5. Discussion

The results in section 4 summarize the general response of the proposed thermal emitter with simultaneous spectral and angular control. In this section, we provide a discussion of other considerations for the TPV system design, including the temperature dependence of optical constants, the separation distance effect, and other practical considerations for experimental realization of the proposed device.

5.1 Practical design considerations

The emitter structure in Fig. 2 is designed to operate at extremely high temperatures. Thus, it is important to make sure that all the involved materials have a melting point well above the operating temperature, since nanostructures tend to melt at lower temperatures than their bulk counterparts [56]. SiO_2 can be used as a low-index material in the filter, with its melting point at 1983 K. The melting point of a highly doped ZnO material, as extracted from [55], can be estimated using the method described in [57]. The estimated new melting point at the given dopant concentration is 2197 K which is still considerably high.

Considering fabricating the structure, standard deposition and lithography techniques can be used to fabricate the bottom and the top structure in Fig. 2. Maintaining the gap between the top and the bottom structure can be realized using periodic mechanical posts spaced at separation distances much larger than the periodicity of the grating. Also, a transparent buffer layer like Silica aerogel can be filled in the gap to maintain mechanical support. Silica aerogel is made of highly porous Silica with a refractive index close to unity, which also exhibit high melting point [58].

5.2 Temperature dependence of optical constants and emissivity

The emitter structure proposed in Fig. 2 involves different materials with expected temperature-dependent optical constants. Hence, it is useful to incorporate theoretical models of this temperature dependence in the optical simulation. For dielectrics, the thermo-optic coefficient is low ($\sim 10^{-6}$ 1/K [59]) so the change in its refractive index is negligible. For Si, three types of temperature-dependent absorption phenomena are significant: bandgap narrowing, above-bandgap absorption, and free-carrier absorption. We use the model presented in [60] that takes these effects into consideration. For Ta and AZO, we use the

Drude-Lorentz model presented in [61] to take temperature effects into consideration via a temperature-dependent plasma frequency $\omega_p(T)$, and damping factor $\Gamma(T)$. This model can be written as:

$$\varepsilon(\omega, T) = \varepsilon_\infty - \frac{\omega_p^2(T)}{\omega^2 - i\omega\Gamma(T)} + \sum_{n=1}^N \frac{\omega_{pn}^2}{\omega_{Tn}^2 - \omega^2 - i\omega\Gamma_{Tn}(T)}, \quad (6)$$

where ε_∞ is the permittivity at infinite frequency, ω is the angular frequency, ω_{Tn} and Γ_{Tn} are the resonance frequency and the damping factor of the n^{th} Lorentz oscillator. The temperature dependence of the plasma frequency $\omega_p(T)$ and the damping factors $\Gamma(T)$ and $\Gamma_{Tn}(T)$ can be expressed as follows:

$$\omega_p(T) = \frac{\omega_p(T_0)}{1 + \alpha(T - T_0)}, \quad (7)$$

$$\Gamma(T) = \Gamma(T_0) \cdot \left(\frac{T}{T_0}\right)^\beta, \quad (8)$$

where α is the thermal expansion coefficient (1/K), β is a general exponent describing the phonon population increase with temperature [62], and T_0 is the reference room temperature (300 K). For both AZO and Ta, the damping factor will show a significant dependence on temperature, which is assumed to be linear to first order. However, the actual value of the exponent β is material-dependent. Comparing AZO to other doped oxides such as Gallium-doped Zinc-oxide and Indium-doped Tin-oxide, AZO has the lowest damping factor at room temperature [55]. Table 1 summarizes the Drude-Lorentz model parameters for both Ta and AZO. The optical parameters of AZO are shown in Fig. 6 at temperatures 300 K, 873 K and 1573 K. As the temperature increases, the real part of the permittivity becomes less negative for longer wavelengths, while the imaginary part increases with temperature.

Table 1. Drude-Lorentz Parameters of Ta and AZO at 300 K (eV)

Material	Ta			AZO ^a		
Drude parameters	ε_∞	ω_p	Γ	ε_∞	ω_p	Γ
	1	7.34153	0.06387	3.5402	1.7473	0.04486
Lorentz parameters	ω_{p1}	ω_{T1}	Γ_{T1}			
	22.465	5.91157	11.913			

^aParameters obtained from [55].

After accounting for the temperature dependence of the optical properties, we plot the emissivity contour plots at three different temperatures: 300 K, 873 K and 1573 K in Fig. 7. They show that the parasitic off-directional losses and spectral parasitic losses increase with temperature. Presumably, off-directional losses result from the change of the optical constants of the AZO, with the real part becoming flatter around the cross-over frequency. In the absence of the filter, Ferrell-Berremann mode and the PA mode become nearly indistinguishable at higher temperatures. Extra losses from the Ta back metal and the Si grating may also contribute to off-directional emission. The increased spectral parasitic losses are mainly caused by the increased ENZ mode spectral width at higher temperature, also in consistence with the observed results in [38]. This also might be a consequence of the AZO

optical parameters temperature dependence at longer wavelengths. It is worth mentioning that the angular dispersion in Fig. 7 is a filter-dependent property, caused by Bragg reflection at different incident angles. In contrast to emissivity plots in [26], Fig. 7 illustrates a complementary response, where the high-emissivity is restricted to a specific range of angles and frequency, with frequency selectivity mainly provided by the filter. However, in [26] a low-emissivity response is restricted to a specific range of angles and frequencies, with the frequency selectivity provided by material absorption.

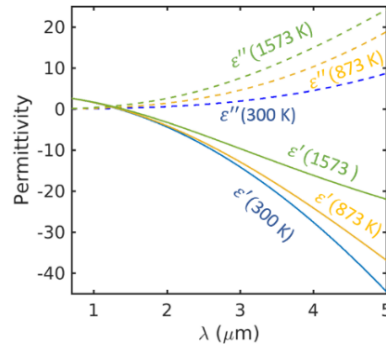


Fig. 6. Temperature dependence of the optical constants of AZO at high temperatures. Drude-model is used to construct this figure, with parameters retrieved from Table. 1 and applying (6), (7) and (8).

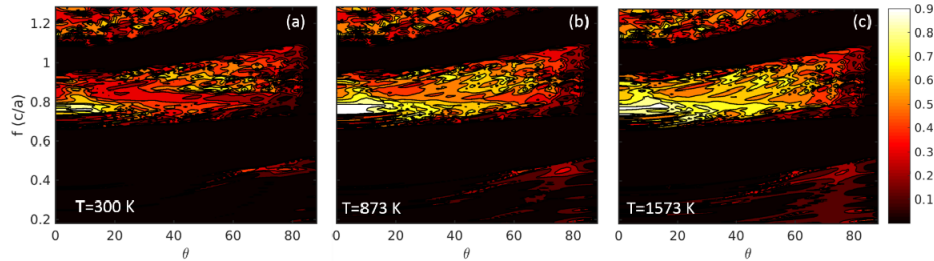


Fig. 7. The change of emissivity function at high temperatures ((b) $T = 873$ K, and (c) $T = 1573$ K) compared to room temperature ((a) $T = 300$ K) parameters. The change of the optical parameters with temperature causes an increase in the parasitic spectral and off-directional radiation, increasing losses of view factor at higher temperatures.

5.3 TPV efficiency

The TPV efficiency is computed as mentioned earlier in section 3.2. The system shown in Fig. 1 is simulated with $l_1 = l_2 = L$, and $D = 1.5L$, with a TPV diode having a unity ideality factor and a unity EQE . Neglecting any changes of the emissivity at high temperatures, we assume an emitter temperature $T_e = 1573$ K. The TPV diode bandgap E_g is swept from 0.8 eV to 1.2 eV to determine the bandgap that maximizes the TPV efficiency. The optimum bandgap can be readily deduced from Fig. 5 near the cut-off of the filter to be around a normalized frequency of $0.78c/a$ (~ 1154 nm). Sweeping the bandgap shows a maximum of 11.66% at 0.92 eV (1348 nm) in Fig. 8(a). The drop in the TPV efficiency above the maximum bandgap is due to shifting the bandgap towards wavelengths shorter than the filter's cut-off wavelength, and thus increasing parasitic losses compared to the useful portion above the bandgap. Below the maximum, the dark current increases exponentially with decreasing bandgap $\sim \exp(-E_g / kT_d)$ where T_d is the diode temperature, thus reducing V_{OC} , and the efficiency. The absolute low efficiency values are mainly caused by the emissivity

beam divergence with distance, which suggests using higher angular restriction for large values of separation distances D .

In terms of the view factor, a planar Lambertian heat source should be placed as close as possible to the receiver to enhance the view factor. In case of directional heat sources, the view factor will also depend on the distance between the emitter and the receiver. The directionality of the source collimates heat radiation towards the receiver, but the beam divergence limits the separation distance. In the proposed design in Fig. 5 and Fig. 7, the halfwidth of the beam is almost 20° , corresponding to rapid divergence. In Fig. 8 (b) and (c), the dependence of the computed TPV efficiency with the separation distance D is plotted. Assuming reasonable values of L that maintain the far-field radiative heat transfer regime ($L > 12$ microns in this case), the plots span values of $D = 0.2L$ to $4.7L$. In this range, near-field heat transfer will not occur to a measurable degree. To quantify the effect of beam divergence, we first plot the TPV efficiency for an ideal emitter that have zero off-directional losses and zero parasitic spectral losses. We assume the same spectral width of the emissivity function in Fig. 5, the same temperature (1573 K) and the same TPV diode parameters at the optimum bandgap obtained in Fig. 8(a). The computed TPV efficiency in Fig. 8(a) shows a significant reduction of the TPV efficiency from 50.48% at $D/L = 0.2$ to 17.9% at $D/L = 4.7$. To further isolate the effect of angular and spectral selectivity, we estimate the contribution of each kind of selectivity alone. For example, in Fig. 8(b), we show the effect of switching off angular selectivity, i.e. extending the emissivity function at 0° over the whole range of angles, while forcing zero sub-bandgap emission. A reduction of the efficiency from 44.58% at $D/L = 0.2$ to 5.22% at $D/L = 4.7$ is found in this case. Likewise, we switch off ideal spectral selectivity by using the same values of the emissivity function in Fig. 5 from 0° to 20° and setting the emissivity to zero otherwise. In this case, a reduction of the efficiency value at $D/L = 0.2$ to 14.3% is noticed because of the increased spectral parasitic losses. At longer distances, the angular selectivity becomes less effective, and drops to almost 5% at $D/L = 4.7$. In all the studied cases, the selectivity in general outperforms the blackbody efficiency at all separation distances. Particularly, at $D/L = 4.7$, the relative enhancement of the TPV efficiency reaches 32% compared to a typical blackbody emitter.

Then, the TPV efficiency is computed for the non-ideal emissivity functions in Fig. 7, and plotted in Fig. 8(c). Using the contour plot in Fig. 7(a), with optical parameters computed at 300 K and assuming an emitter temperature of 1573 K, the TPV efficiency drops to 28.15% at $D/L = 0.2$. This significant reduction is caused by increased spectral and angular parasitic losses. At longer distances, the losses increase as the beam diverges more reaching 4.055% at $D/L = 4.7$. To further estimate the enhancement due to angular selectivity alone, we switch off angular selectivity, by just extending the spectrum at 0° over the whole range of angles. We notice an average enhancement of 1.13x added by the angular selectivity. Compared to a blackbody at the same temperature, Fig. 7(a) results in larger enhancement as the separation distance increases, and shows an average enhancement factor of 7.2058x. It is also noticeable that the angular selectivity reduces the efficiency at shorter distances, because of the reduced collected emission with angular restriction compared to omni-directional emission.

Finally, using the contour plot in Fig. 7(c), i.e. with optical parameters computed at 1573 K, the efficiency is reduced to 20.52% at short separation distances and to 2.91% at a distance of $D/L = 4.7$. The average enhancement added by angular selectivity is reduced to 1.0861x. This reduction is due to the increased parasitic off-directional and spectral losses. Comparing to a blackbody at the same temperature, Fig. 7(c) results in a reduced average enhancement factor of 5.38x, and particularly, 3.9% relative enhancement compared to the blackbody at $D/L = 4.7$. From Fig. 8(b), it is obvious that the increased parasitic losses, both angular and spectral, weakens the benefit of angular selectivity. The results in Fig. 8(b) and 8(c) suggests that the proposed design in Fig. 1 is susceptible to angular parasitic losses. Thus, a requirement of a sharp angular selectivity may be difficult to obtain and maintain in realistic situations.

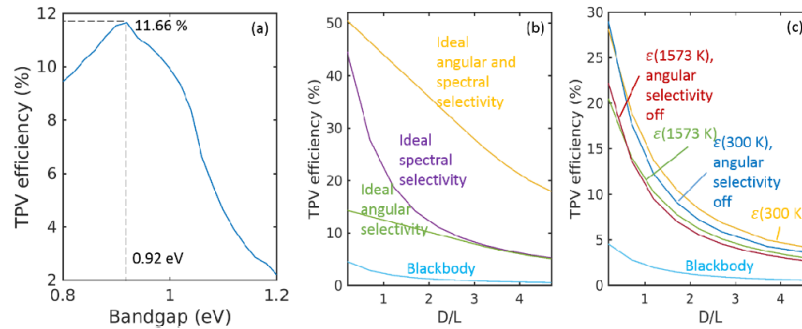


Fig. 8. (a) The computed TPV efficiency as a function of the TPV diode bandgap. The separation distance between the emitter and the receiver is set to $D = 1.5l_1 = 1.5l_2$. The figure shows a maximum TPV efficiency of 11.66% at a PV bandgap of 0.92 eV. (b), (c) Plots of the TPV efficiency dependence with distance D : (b) using an ideal spectral and angular selective emitter, with zero sub-bandgap losses and zero off-directional losses: The highest efficiencies can be extracted from an emitter with ideal spectral and angular selectivity, and (c) using the designed selective emitter with different temperature optical parameters.

6. Summary

We have presented a design of a thermal emitter exhibiting simultaneous control of angular and spectral properties for TPV application. Spectral selectivity allows for higher potential TPV efficiencies. Angular restriction enables much higher view factors at significantly greater separations. These objectives are achieved utilizing resonant absorption phenomena in ENZ thin-films coupled through a grating structure. The TPV system efficiency is computed for angular and spectral selective thermal emission. A relative enhancement of 3.9% over a blackbody emitter at the same emitter temperature and receiver conditions has been achieved. Despite the small enhancement factor, the absolute efficiency can still reach ~5% at large separation distances (5 times the emitter size) that are still suitable for compact TPV devices. This enhancement factor increases at shorter separation distances and lower beam divergence. With the presence of parasitic spectral and angular emission, the TPV efficiency drops significantly compared to an emitter with ideal angular and spectral selectivity. The results suggest that eliminating off-angular and parasitic spectral emission could potentially result in a relative enhancement of the TPV efficiency up to 32% over a blackbody at large separation distances. The presented study shows the potential value of simultaneous spectral and angular selectivity, offering more flexibility in designing high efficiency, reliable TPV systems.

Funding

Department of Energy (DOE) (DE-EE0004946); Northrop Grumman Aerospace Systems (301613); National Science Foundation (NSF) (EEC-1454315, EEC-0228390).

Acknowledgments

The authors would like to thank Muhammed A. Alam, Zhiguang Zhou and David Kortge for useful discussions. The authors also thank Deanna Dimonte and Shailja Dhaka for assistance in developing useful codes.